SAPAVE: an improved semi-analytical FE program for dynamic viscoelastic analysis of asphalt pavement

Kairen Shen , Hao Wang , Hanyu Zhang , Jusheng Tong & Xianhua Chen

Published online: 03 Feb 2021.

Submit your article to this journal

View related articles

View Crossmark data

Taylor & Francis
Taylor & Francis Group

Check for updates

SAPAVE: an improved semi-analytical FE program for dynamic viscoelastic analysis of asphalt pavement

Kairen Shen [a,b], Hao Wang [b], Hanyu Zhang [a], Jusheng Tong[a] and Xianhua Chen [a]

aSchool of Transportation, Southeast University, Nanjing, People's Republic of China; bDepartment of Civil and Environmental Engineering, Rutgers, State University of New Jersey, Piscataway, NJ, USA

ABSTRACT

Analyzing dynamic viscoelastic responses induced by moving loads is a significant issue for pavement design and performance evaluation. Developing three-dimensional FE models in commercial software is an effective method, but the time-consuming disadvantage prevents it from extensive engineering applications. In this paper, an improved semi-analytical FE model was proposed to overcome this drawback. Besides, modified artificial boundaries were applied to minimise the interference of reflected waves generated by model edges. Further, a program named SAPAVE has been developed in MATLAB to achieve the modeling procedure, of which accuracy and efficiency were verified by comparing with the three-dimensional FE model in ABAQUS. The computing cost of SAPAVE was only one-sixth of ABAQUS, while SAPAVE can roughly achieve the function of ABAQUS for simple pavement modeling. The response considering the asphalt layer as viscoelastic was quite different from the linear elastic in the comparative study. The viscoelastic analysis seems to be closer to the field situation. Besides, the impact of vehicle speed was studied to examine the application ability of SAPAVE, and the results were generally consistent with existing researches. Overall, this study indicates that SAPAVE is an efficient and accurate tool for mechanical analysis of asphalt pavement.

1. Introduction

Analyzing dynamic response induced by moving loads is of great importance for pavement design and performance evaluation. Finite element method (FEM) is a practical approach to simulate the dynamic process. In general, pavement modeling consists of selecting appropriate dimensions of finite domain and the degree of its discretisation to represent dynamic behavior of semi-infinite space.

The three-dimensional (3D) FEM is capable of building comprehensive model for real pavement structures (Helwany et al. 1998, Saad et al. 2005). However, the computing cost increases with the complexity and may exceed the computer capability sometimes. This disadvantage is further highlighted in dynamic viscoelastic analysis due to its iteration of viscoelastic integrals and dynamic analysis steps. Since the computation mainly derives from the matrix operation of equilibrium equations in 3D domain, dimensionality reduction is a feasible way to improve computing speed.

Asphalt pavement is a multi-layered system, of which the structural geometry and material properties usually do not vary along the direction of vehicular loading. Thus, it is improper to use two-dimensional (2D) plane strain model, which can not represent the moving loads (Myers et al. 2001). However, the semi-analytical FEM (SAFEM) conducts meshing in the cross-section and substitutes meshing with the interpolation of Fourier series along the driving direction (Zienkiewicz and Too 1972), which can simulate the loading discontinuity with the capability of Fourier series to represent any continuous functions. Each Fourier series term corresponds to a plane strain problem, and the actual result can be synthesised from all 2D solutions by the inverse Fourier transform (Zienkiewicz and Taylor 2005). It can also obtain the mechanical state in 3D space by substituting arbitrary longitudinal coordinates into the transform. Figure 1 presents the three FE models, 2D FEM, SAFEM, and 3D FEM, in terms of accuracy and computation time. It can be found that SAFEM is an appropriate simplication for simulation of 3D pavement.

Zienkiewicz and Too first summarised the SAFEM and verified its accuracy by the elastic prismatic bar analysis (Zienkiewicz and Too 1972). Gradually, this method has been in utilisation for pavement modeling over the past two decades. Jooste first introduced SAFEM for static elastic analysis of pavement, which possessed more analytical functions than the traditional elastic layered system (Jooste 2002). Hu et al. further embedded the crack element in static analysis of SAFEM to develop a program called SA-CrackPro, which calculated the stress intensity factor of the crack tip under static loads (Hu et al. 2008, Wu et al. 2014). This study also showed that SAFEM has a good alienation ability for particular issues, which is one of the advantages of numerical methods over traditional analytical methods. Liu et al. developed SAFEM program for dynamic elastic analysis of pavement under moving loads, and verified the accuracy and efficiency by comparing with 3D FEM developed with ABAQUS (Liu et al. 2017, Liu et al. 2018a). Using the Burgers model to characterise the material properties, Liu et al. further developed SAFEM to
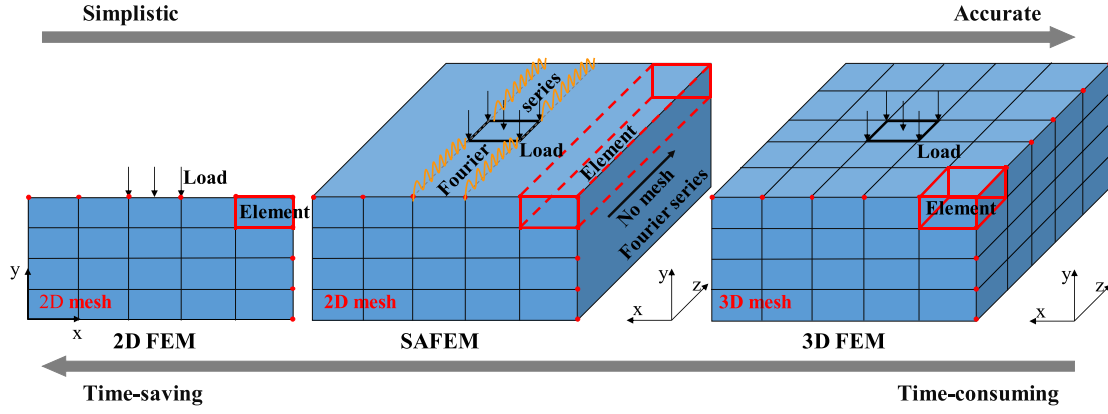
Figure 1. Comparison of three typical FE models.

simulate flexible pavement creep deformation under static loads (Liu *et al.* 2018b).

It is worth noting that few studies of SAFEM concerning pavement modeling involve dynamic viscoelastic analysis, while this issue is important for accurately calculating asphalt pavement responses induced by vehicular loads. The reason is that viscoelasticity can account for the relationship between mechanical properties of asphalt mixture with loading time (Moita et al. 2011) and the creep recovery behavior after unloading (Kim 2011), while elastic analysis ignores these realities.

Moreover, dynamic analysis requires appropriate artificial boundaries because waves generated by moving loads and propagating inside the pavement will be reflected at the boundaries and influence wave propagation (Beskou et al. 2016a, 2016b). In existing researches, the boundary conditions are usually set as fixing node displacements or freeing boundary nodes (Jooste 2002, Hu et al. 2008, Liu et al. 2017, Liu *et al.* 2018a). This method may be suitable for static analysis, but the propagation effect generated by boundaries cannot be neglected in dynamic analysis. Besides, some studies coupled finite and infinite elements to reduce the influence of boundaries (Liu et al. 2015). Nevertheless, this method increases calculation time because the infinite elements add the matrix dimension of equilibrium equations. In summary, the current state-of-practice of using SAFEM for pavement analysis is illustrated in Figure 2.

2. Objective

This study aims to improve model formulation of SAFEM and develop an analytical program for dynamic viscoelastic analysis of asphalt pavement under moving loads. Improved artificial boundary conditions are proposed and implemented in this model. A program named SAPAVE is developed in MATLAB, of which the accuracy and efficiency are verified by comparing with 3D FEM in ABAQUS.

3. Method and program description

3.1. SAFE model

SAFEM only requires meshing in the cross-section and uses the Fourier series to represent the component along the driving direction of all variables. The SAFE model of pavement structure is illustrated in Figure 3. Let (x, y, z) be the coordinates describing the domain. The driving direction z, along which the geometry and material properties do not change, is limited to lie between two values $(0 \leq z \leq a)$. Because the Fourier series can represent any continuous function, the displacement $\mathbf{u}$ defined by shape functions $\mathbf{N}$ has a separation form as follows:

$$\mathbf{u} = \sum_{i=1}^{n} \mathbf{N}_i(x, y, z)\mathbf{u}_i$$

$$= \sum_{l=1}^{L} \sum_{i=1}^{n} \left[\mathbf{N}_{si}(x, y)sin\frac{l\pi z}{a} + \mathbf{N}_{ci}(x, y)\cos\frac{l\pi z}{a} \right]\mathbf{u}_i^l \quad (1)$$

where i is node number in element, l is the lth Fourier series term, and $\mathbf{u}^l$ is the corresponding displacement component. Besides, it is naturally assumed that the shape functions $\mathbf{N}_s$ and $\mathbf{N}_c$ in the domain (x, y) are the same as those of 2D FEM.
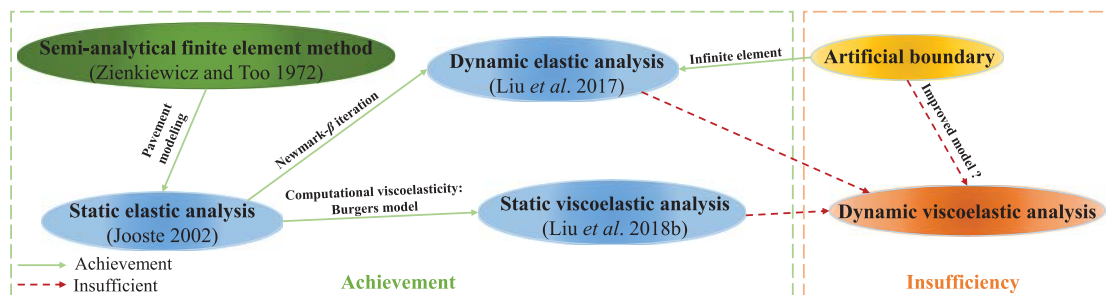

Figure 2. The achievement and insufficiency of SAFEM utilised in modeling pavement.
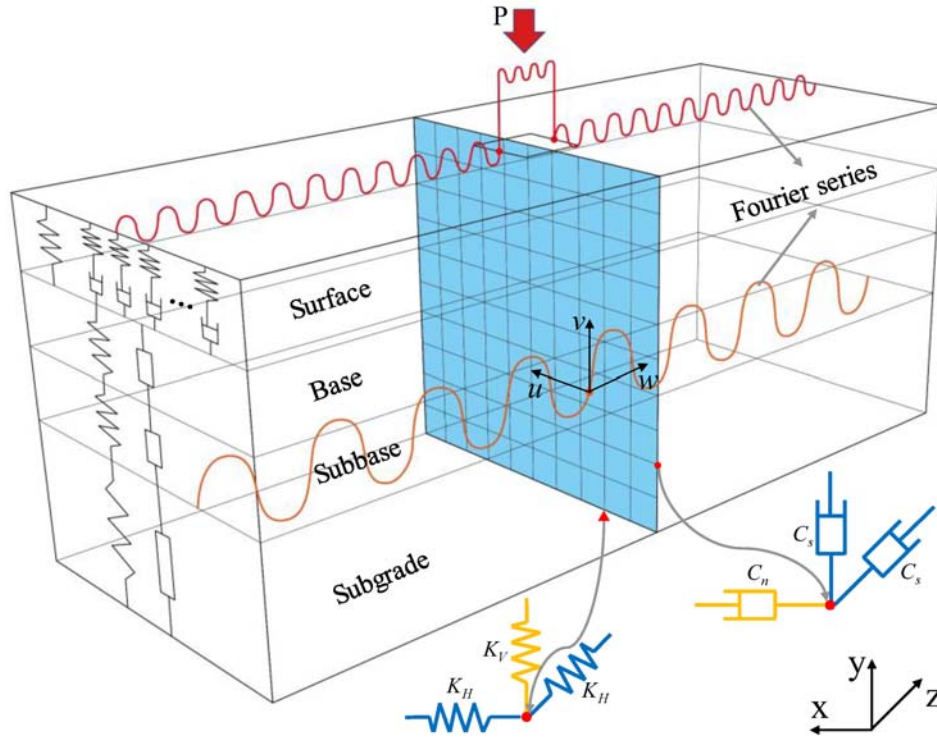
Figure 3. Schematic representation of the SAFE model of pavement.

3.2. Material model

3.2.1. Viscoelastic material

This study assumes that pavement materials do not generate any damages due to moving loads lasting for a short time. The Boltzmann superposition principle can represent the stress–strain relationship as a convolution integral as follows (Markovitz 1977):

$$\sigma(t) = \int_0^t E(t - \tau) \frac{\partial \varepsilon}{\partial \tau} d\tau \tag{2}$$

where, t is the current time, and τ is a time parameter.

The asphalt surface is assumed as linear viscoelastic material in this study, and the Generalised Maxwell model (GMM) represents its mechanical property. Thus, the Prony series of relaxation modulus $E(t)$ has the following form:

$$E(t) = E_\infty + \sum_{i=1}^n E_i e^{-E_i t / \eta_i} = E_\infty + \sum_{i=1}^n E_i e^{-t/T_i} \tag{3}$$

where, E_∞, E_i, and η_i are the coefficients of the components illustrated in Figure 4. Besides, the damping effect of the asphalt mixture is already considered by the dashpots in the GMM.

3.2.2. Elastic material

For base, subbase, and soil, the stress–strain relationship is characterised as isotropic elasticity, and the damping effects should be considered due to the energy dissipation in these structures (Chen and Russell 1982). This study adopts the Rayleigh damping model to represent the damping effects as follows:

$$\mathbf{C} = \alpha \mathbf{M} + \beta \mathbf{K} \tag{4}$$

where $\mathbf{C}$, $\mathbf{M}$, and $\mathbf{K}$ are damping, mass, and stiffness matrixes, respectively; α and β are the Rayleigh coefficients can be calculated as follows:

$$\alpha = \xi \frac{2\omega_i \omega_j}{\omega_i + \omega_j} \;\&\; \beta = \xi \frac{2}{\omega_i + \omega_j} \tag{5}$$

where ξ is the damping ratio, ω_i and ω_j are the critical frequencies.

3.3. Boundary condition

The vertical and bottom faces are artificial boundaries, of which inappropriate settings would reflect the propagating wave generated by moving loads inside the pavement domain. Then, the reflected waves will pollute the wave propagation.
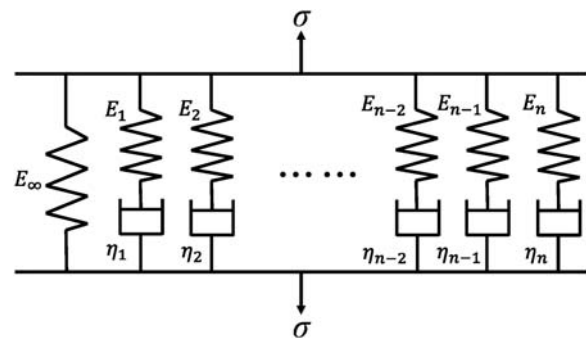

Figure 4. Schematic representation of the Generalised Maxwell model.

Thus, it is necessary to minimise the interference of reflected waves by setting a reasonable boundary.

3.3.1. Left and right vertical boundaries

To control the interference of reflected waves, absorbing or non-reflecting devices can be applied at the vertical edge. This study adopts the viscous device proposed by Hatzigeorgiou and Beskos (Hatzigeorgiou and Beskos 2010), that is widely used for computational efficiency. The fundamental is applying traction at artificial boundaries to make any reflected stresses become zero, which is represented as follows:

$$T_n + \alpha_T \rho V_n \dot{u}_n = 0 \ \& \ T_s + \beta_T \rho V_s \dot{u}_s = 0 \quad (6)$$

where, T_n and T_s are the normal and shear tractions respectively; $\dot{u}_n$ and $\dot{u}_s$ are the normal and tangential velocities respectively; α_T and β_T are dimensionless parameters usually taken as 1; ρ is the density of materials; V_n and V_s are the normal and shear propagation wave velocities respectively, which can be obtained as follows:

$$V_n = \sqrt{\frac{E(1-\nu)}{(1+\nu)(1-2\nu)\rho}} \ \& \ V_s = \sqrt{\frac{E}{2(1+\nu)\rho}} \quad (7)$$

3.3.2. Front and rear vertical boundaries

Generally, Fourier series with only odd or even expansions can also represent continuous functions (Tolstov 2012). Besides, if the length of driving direction is long enough, it is reasonable to prevent displacements in the x-y plate but permit free motion in the z coordinate at the front and rear boundary ($z = 0$ and $z = a$). These boundary conditions can be fulfilled by adopting only odd or even expansion of the Fourier series. This simplification is of great significance for reducing the calculation amount by half theoretically. Then the displacement $\mathbf{u}$ consisting of three parts (u, v, and w) can be written as follows:

$$\mathbf{u} = \begin{Bmatrix} u \\ v \\ w \end{Bmatrix} = \sum_{l=1}^{L} \sum_{k=1}^{I} \begin{Bmatrix} N_s(x,y)\sin\dfrac{l\pi z}{a} u_k^l \\ N_s(x,y)\sin\dfrac{l\pi z}{a} v_k^l \\ N_c(x,y)\cos\dfrac{l\pi z}{a} w_k^l \end{Bmatrix}$$

$$= \sum_{l=1}^{L} \mathbf{N}^l \mathbf{u}^l \quad (8)$$

3.3.3. Bottom boundary

Spring devices can be set at the bottom face to simulate the soil medium supporting. The horizontal and vertical spring constants K_H and K_V proposed by Mulliken and Karabalis (Mulliken and Karabalis 1998) can be utilised as follows:

$$K_H = \frac{4.6EL_S}{(1+\nu)(2-\nu)} \ \& \ K_V = \frac{2.35EL_S}{(1-\nu^2)} \quad (9)$$

where, L_S is the half-length of the equivalent square side of the contact face, which can be calculated as follows:

$$L_S = \sqrt{D_S}/2 \quad (10)$$

Where, D_S is the area of the contact face.

3.4. Global equilibrium equation

The pavement domain should resemble neither a beam nor a plate, but rather a cube-like solid (Huang 2004). Therefore, it is difficult to derive the equilibrium equation of this system by theoretical mechanics. Generally, the pavement domain Ω can be regarded as a closed system, and the principle of virtual work is applicable to establish the equilibrium equation (de Araújo et al. 2010). The numerical formulation of dynamic viscoelastic analysis of pavement structure based on virtual work principle can be represented.

Here, δW_S, δW_I, δW_D, δW_b, δW_L, and δW_B respectively are the virtual work done by the stress field, inertia forces, damping force, body force, applied loads, and boundary function on a virtual strain $\delta\boldsymbol{\varepsilon}$, which can be written as follows:

$$\delta W_S = \int_\Omega [\delta\boldsymbol{\varepsilon}(t)]^T \boldsymbol{\sigma}(t) d\Omega$$

$$\delta W_I = -\int_\Omega [\delta\mathbf{u}(t)]^T \rho \ddot{\mathbf{u}}(t) d\Omega$$

$$\delta W_D = -\int_\Omega [\delta\mathbf{u}(t)]^T c \dot{\mathbf{u}}(t) d\Omega$$

$$\delta W_b = \int_\Omega [\delta\mathbf{u}(t)]^T \mathbf{g} d\Omega \quad (11)$$

$$\delta W_L = \int_\Gamma [\delta\mathbf{u}(t)]^T \mathbf{F}_L(t) d\Gamma$$

$$\delta W_B = \int_\Gamma [\delta\mathbf{u}(t)]^T \mathbf{F}_B(t) d\Gamma$$

where $\mathbf{u}$, $\dot{\mathbf{u}}$ and $\ddot{\mathbf{u}}$ are the displacement, velocity, and acceleration vectors, respectively; c is the damping coefficients of materials; $\mathbf{g}$, $\mathbf{F}_L(t)$ and $\mathbf{F}_B(t)$ are the gravity, applied load, and condition function, respectively.

According to the principle of virtual work, one can obtain the following equation:

$$\delta W_S = \delta W_I + \delta W_D + \delta W_b + \delta W_L + \delta W_B \quad (12)$$

The displacement vector within each element can be taken as a function of the nodal displacement, and the velocity and acceleration vector have the same forms as follows:

$$\mathbf{u}(t) = \sum_{i=1}^{n} \mathbf{N}_i \mathbf{u}_i(t)$$

$$\dot{\mathbf{u}}(t) = \sum_{i=1}^{n} \mathbf{N}_i \dot{\mathbf{u}}_i(t) \quad (13)$$

$$\ddot{\mathbf{u}}(t) = \sum_{i=1}^{n} \mathbf{N}_i \ddot{\mathbf{u}}_i(t)$$

where $\mathbf{N}_i$, $\mathbf{u}_i$, $\dot{\mathbf{u}}_i$ and $\ddot{\mathbf{u}}_i$ are the shape function matrix and corresponding node variables.

By differentiating node displacement concerning reference coordinates, the strain-displacement relation becomes the

following:

$$\boldsymbol{\varepsilon}(t) = \mathbf{B}\mathbf{u}_i(t) \tag{14}$$

where B is the strain-displacement matrix.

Substituting Equations (13), (14) into Equation (12) obtains the global equilibrium equation:

$$\int_{\Omega} \mathbf{B}^T \boldsymbol{\sigma}(t) d\Omega + \int_{\Omega} \mathbf{N}^T \rho \mathbf{N} \ddot{\mathbf{u}}_i(t) d\Omega + \int_{\Omega} \mathbf{N}^T c \mathbf{N} \dot{\mathbf{u}}_i(t) d\Omega$$
$$= \int_{\Omega} \mathbf{N}^T \mathbf{g} d\Omega + \int_{\Gamma} \mathbf{N}^T [\mathbf{F}_L(t) + \mathbf{F}_B(t)] d\Gamma \tag{15}$$

3.5. Numerical solution method

3.5.1. Finite element and shape function
The four-node isoparametric rectangle element is used to mesh the model, and the Langrage shape function in local coordinates (ξ, η) is set as follows:

$$N_1(\xi, \eta) = \frac{1}{4}(1 - \xi)(1 - \eta)$$
$$N_2(\xi, \eta) = \frac{1}{4}(1 + \xi)(1 - \eta)$$
$$N_3(\xi, \eta) = \frac{1}{4}(1 + \xi)(1 + \eta) \tag{16}$$
$$N_4(\xi, \eta) = \frac{1}{4}(1 - \xi)(1 + \eta)$$

Then, the shape function matrix of a SAFE element under lth terms of the Fourier series can be written as follows:

$$\mathbf{N}^l = [\mathbf{N_1} \quad \mathbf{N_2} \quad \mathbf{N_3} \quad \mathbf{N_4}]$$

$$= \begin{bmatrix} N_1 \sin\frac{l\pi z}{a} & 0 & 0 & N_4 \sin\frac{l\pi z}{a} & 0 & 0 \\ 0 & N_1 \sin\frac{l\pi z}{a} & 0 & \cdots & 0 & N_4 \sin\frac{l\pi z}{a} & 0 \\ 0 & 0 & N_1 \cos\frac{l\pi z}{a} & 0 & 0 & N_4 \cos\frac{l\pi z}{a} \end{bmatrix} \tag{17}$$

The strain-displacement matrix of an element $\mathbf{B}_e^l$ can be obtained by a similar method, as shown below:

$$\mathbf{B}_e^l = [\mathbf{B_1} \quad \mathbf{B_2} \quad \mathbf{B_3} \quad \mathbf{B_4}]$$

$$\mathbf{B}_i = \begin{bmatrix} \frac{\partial N_i}{\partial x}\sin\frac{l\pi z}{a} & 0 & 0 \\ 0 & \frac{\partial N_i}{\partial y}\sin\frac{l\pi z}{a} & 0 \\ 0 & 0 & -\frac{l\pi}{a}N_i\sin\frac{l\pi z}{a} \\ \frac{\partial N_i}{\partial y}\sin\frac{l\pi z}{a} & \frac{\partial N_i}{\partial x}\sin\frac{l\pi z}{a} & 0 \\ 0 & \frac{l\pi}{a}N_i\cos\frac{l\pi z}{a} & \frac{\partial N_i}{\partial y}\cos\frac{l\pi z}{a} \\ \frac{l\pi}{a}N_i\cos\frac{l\pi z}{a} & 0 & \frac{\partial N_i}{\partial x}\cos\frac{l\pi z}{a} \end{bmatrix} \tag{18}$$

Setting $\mathbf{K}^{lm} = \int_{\Omega} (\mathbf{B}_e^l)^T \mathbf{D} \mathbf{B}_e^m d\Omega$, the stiffness of an element can

be written as follows:

$$\mathbf{K}^e = \int_{\Omega} \mathbf{B}_e^T \mathbf{D} \mathbf{B}_e d\Omega = \begin{bmatrix} \mathbf{K}^{11} & \cdots & \mathbf{K}^{1L} \\ \vdots & \ddots & \vdots \\ \mathbf{K}^{L1} & \cdots & \mathbf{K}^{LL} \end{bmatrix} \tag{19}$$

Due to the $\mathbf{B}_e^l$, $\mathbf{K}^e$ includes the following integrals:

$$I_1 = \int_0^a \sin\frac{l\pi z}{a}\sin\frac{m\pi z}{a}dz \ \& \ I_2 = \int_0^a \cos\frac{l\pi z}{a}\cos\frac{m\pi z}{a}dz$$

$$I_1 = I_2 = \begin{cases} \frac{1}{2}a, l = m \\ 0, \quad l \neq m \end{cases}$$

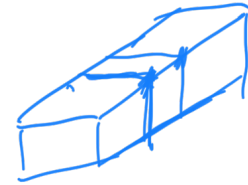Thus, $\mathbf{K}^e$ becomes a block diagonal matrix as follows:

$$\mathbf{K}^e = diag(\mathbf{K}^{11}, \cdots, \mathbf{K}^{LL}) \tag{21}$$

This is also the essential of SAFEM, which transforms a 3D matrix into L independent 2D matrixes (Zienkiewicz and Taylor 2005). It also means that the original 3D FEM is transformed into L independent 2D FEM.

Further, four Gauss points setting in local coordinates are adopted to solve the integral $\mathbf{K}^{ll} = \frac{a}{2}\int_A \bar{\mathbf{B}}^T \mathbf{D}\bar{\mathbf{B}}dxdy$, and all Gauss points have unit weight $W_i = 1$. Besides, using Jacobian operator $\mathbf{J}$ transforms all variables from local coordinates into global coordinates. This calculation process can be expressed as follows:

$$\mathbf{K}^{ll} = \frac{a}{2}\int_A \bar{\mathbf{B}}^T \mathbf{D}\bar{\mathbf{B}}dxdy = \sum_{i=1}^4 \frac{a}{2}\bar{\mathbf{B}}^T \mathbf{D}\bar{\mathbf{B}}W_i \det\mathbf{J} \tag{22}$$

Further, according to the element number, global stiffness matrix can be assembled. Moreover, other matrixes also adopt similar calculation methods.

3.5.2. Numerical solution of stress integral
The stress integral consists of elastic and viscoelastic parts. For the elastic parts contributed from the base, subbase, and soil, the integral has the following form:

$$\int_{\Omega} \mathbf{B}^T \boldsymbol{\sigma}(t) d\Omega = \int_{\Omega} \mathbf{B}^T \mathbf{D}\mathbf{B}d\Omega\mathbf{u}(t) = \sum_{l=1}^L \mathbf{K}_0^{ll}\mathbf{u}^l(t) \tag{23}$$

For the asphalt mixture, the viscoelastic stress has the following form:

$$\boldsymbol{\sigma}(t) = \mathbf{S}(t) + \boldsymbol{\sigma}_0(t)$$
$$= 2\int_0^t G(t - \tau)\frac{\partial \mathbf{e}(\tau)}{\partial \tau}d\tau + 3\int_0^t K(t - \tau)\frac{\partial \boldsymbol{\varepsilon}_0(\tau)}{\partial \tau}d\tau \tag{24}$$

Dividing time t into n equal parts, let the subscripts of variables at each time be $1 \sim n+1$. The first integral has the following form:

$$\mathbf{S}_{n+1} = \mathbf{S}_n + 2\int_{t-\Delta t}^{t} G(t-\tau)\frac{\partial \mathbf{e}}{\partial \tau}d\tau$$
$$+ \sum_{i=1}^{n} 2G_i(e^{-\Delta t/T_i} - 1)\int_{0}^{t-\Delta t} e^{-(t-\Delta t-\tau)/T_i}\frac{\partial \mathbf{e}}{\partial \tau}d\tau \quad (25)$$

Using the trapezoidal integral method (Kaliske and Rothert 1997) to solve the first integral as follows:

$$\int_{t-\Delta t}^{t} G(t-\tau)\frac{\partial \mathbf{e}}{\partial \tau}d\tau \approx \int_{t-\Delta t}^{t} G(t-\tau)d\tau\frac{\mathbf{e}_{n+1} - \mathbf{e}_n}{\Delta t} \quad (26)$$

For the second integral $\mathbf{P}_n^i = \int_0^{t-\Delta t} e^{-(t-\Delta t-\tau)/T_i}\frac{\partial \mathbf{e}}{\partial \tau}d\tau$, one can obtain the following form:

$$\mathbf{P}_n^i \approx e^{-\Delta t/T_i}\mathbf{P}_{n-1}^i + \int_{t-2\Delta t}^{t-\Delta t} e^{-(t-\Delta t-\tau)/T_i}d\tau\frac{\mathbf{e}_n - \mathbf{e}_{n-1}}{\Delta t} \quad (27)$$

For the integral $\mathbf{Q}_n^i = \int_0^{t-\Delta t} e^{-(t-\Delta t-\tau)/T_i}\frac{\partial \boldsymbol{\varepsilon}_0}{\partial \tau}d\tau$, the same relationship can be obtained. It can be found that $\mathbf{P}_n^i$ and $\mathbf{Q}_n^i$ are known variables relating to displacement vectors $\mathbf{u}_1 \sim \mathbf{u}_n$.

Then, using the Newton-Cotes formula (Kalogiratou and Simos 2003) to solve the integral, which exerts more accuracy than Euler's formula:

$$Cotes(G) = \int_{t-\Delta t}^{t} G(t-\tau)d\tau = \frac{1}{90}[90G_\infty + \sum_{i=1}^{n} G_i(7 + 32e^{-0.25\Delta t/T_i} + 12e^{-0.5\Delta t/T_i} + 32e^{-0.75\Delta t/T_i} + 7e^{-\Delta t/T_i})]$$

$$Cotes(K) = \int_{t-\Delta t}^{t} K(t-\tau)d\tau = \frac{1}{90}[90K_\infty + \sum_{i=1}^{n} K_i(7 + 32e^{-0.25\Delta t/T_i} + 12e^{-0.5\Delta t/T_i} + 32e^{-0.75\Delta t/T_i} + 7e^{-\Delta t/T_i})]$$

$$Cotes(e) = \int_{t-2\Delta t}^{t-\Delta t} e^{-(t-\Delta t-\tau)/T_i}d\tau = \frac{1}{90}(7 + 32e^{-0.25\Delta t/T_i} + 12e^{-0.5\Delta t/T_i} + 32e^{-0.75\Delta t/T_i} + 7e^{-\Delta t/T_i})$$

$$(28)$$

Assuming $\mathbf{e}(t) = \mathbf{k}_1\mathbf{B}\mathbf{u}(t)$, $\boldsymbol{\varepsilon}_0(t) = \mathbf{k}_2\mathbf{B}\mathbf{u}(t)$, one can obtain the following form:

$$\boldsymbol{\sigma}_{n+1} \approx \boldsymbol{\sigma}_n + 2Cotes(G)\mathbf{k}_1\mathbf{B}\frac{\mathbf{u}_{n+1} - \mathbf{u}_n}{\Delta t} + 2\sum_{i=1}^{n} G_i(e^{-\Delta t/T_i} - 1)\mathbf{P}_n^i$$

$$+ 3Cotes(K)\mathbf{k}_2\mathbf{B}\frac{\mathbf{u}_{n+1} - \mathbf{u}_n}{\Delta t} + 3\sum_{i=1}^{n} K_i(e^{-\Delta t/T_i} - 1)\mathbf{Q}_n^i$$

$$= \mathbf{K}_1\mathbf{B}\mathbf{u}_{n+1} + \mathbf{K}_2\mathbf{B}\mathbf{u}_{1\sim n}$$

The viscoelastic stress integral has the following form:

$$\int_\Omega \mathbf{B}^T\boldsymbol{\sigma}(t)d\Omega = \int_\Omega \mathbf{B}^T[\mathbf{K}_1\mathbf{B}\mathbf{u}_{n+1} + \mathbf{K}_2\mathbf{B}\mathbf{u}_{1\sim n}]d\Omega$$
$$= \sum_{l=1}^{L}[\mathbf{K}_1^{ll}\mathbf{u}_{n+1}^l + \mathbf{K}_2^{ll}\mathbf{u}_{1\sim n}^l] \quad (30)$$

3.5.3. Numerical solution of other integrals

For damping and inertia stress integral, using a similar method, one can obtain:

$$\int_\Omega \mathbf{N}^T\rho\mathbf{N}d\Omega\ddot{\mathbf{u}}_i(t) = \mathbf{M}\ddot{\mathbf{u}}(t) = \sum_{l=1}^{L}\mathbf{M}^{ll}\ddot{\mathbf{u}}^l(t)$$
$$\int_\Omega \mathbf{N}^T c\mathbf{N}d\Omega\dot{\mathbf{u}}_i(t) = \mathbf{C}\ddot{\mathbf{u}}(t) = \sum_{l=1}^{L}\mathbf{C}^{ll}\dot{\mathbf{u}}^l(t)$$

$$(31)$$

Considering the vertical function of loads only and expressing the load motion as the translation of trigonometric functions, the loading function is obtained as follows:

$$\mathbf{F}_L(t) = \left\{\begin{array}{c} 0 \\ \mathbf{p}(x, y) \\ 0 \end{array}\right\} = \sum_{l=1}^{L}\sum_{i=1}^{n}(\frac{2P_i}{l\pi})[\cos(\frac{l\pi}{a}Z_{i1})$$
$$- \cos(\frac{l\pi}{a}Z_{i2})]\sin\frac{l\pi z}{a}\mathbf{Y}_L$$

$$Z_i(t) = Z_i(0) + V_Lt$$

$$(32)$$

where i is the number of loads, P_i is the ith load pressure; Z_{i1} and Z_{i2} are the coordinates where the load starts and ends, respectively; V_L is the loading velocity; $\mathbf{Y}_L$ is the load vector, of which corresponding elements take 1 when the node acted on a load.

Further, the load stress can be solved as:

$$\int_\Gamma \mathbf{N}^T\mathbf{F}_L(t)d\Gamma = \sum_{l=1}^{L}\sum_{t=1}^{n}(\frac{2P_t}{l\pi})[\cos(\frac{l\pi}{a}Z_{t1})$$
$$- \cos(\frac{l\pi}{a}Z_{t2})]\int_\Gamma \mathbf{N}^T\sin\frac{l\pi z}{a}\mathbf{Y}d\Gamma = \sum_{l=1}^{L}\mathbf{F}_L^l$$

$$(33)$$

The body force stress has the following form:

$$\int_\Omega \mathbf{N}^T\mathbf{g}d\Omega = \sum_{l=1}^{L}9.8\mathbf{M}^{ll}\mathbf{Y}_b = \sum_{l=1}^{L}\mathbf{F}_b^l \quad (34)$$

By treating the bottom boundary as nodal line loads along the driving direction, the boundary function is expressed as:

$$\mathbf{F}_{Bb}^{e}(t) = -\sum_{l=1}^{L} \left\{ \begin{array}{c} K_H u^l \sin\dfrac{l\pi z}{a}/a \\ K_V v^l \sin\dfrac{l\pi z}{a}/a \\ K_H w^l \cos\dfrac{l\pi z}{a}/a \end{array} \right\} \tag{35}$$

Then the integral in Equation (15) has the following form:

$$\int_{\Gamma} \mathbf{N}^T \mathbf{F}_{Bb}(t) d\Gamma = \sum_{l=1}^{L} \mathbf{K}_3^{ll} \mathbf{u}(t)^l \tag{36}$$

Similarly, the vertical boundary can also be treated as nodal line loads as follows:

$$\mathbf{F}_{Bv}^{e}(t) = -\sum_{l=1}^{L} \left\{ \begin{array}{c} \rho V_n r \dot{u}^l \sin\dfrac{l\pi z}{a} \\ \rho V_s r \dot{v}^l \sin\dfrac{l\pi z}{a} \\ \rho V_s r \dot{w}^l \cos\dfrac{l\pi z}{a} \end{array} \right\} \tag{37}$$

where r is the height of the element.

Then the integral in Equation (15) has the following form:

$$\int_{\Gamma} \mathbf{N}^T \mathbf{F}_{Bv}(t) d\Gamma = \sum_{l=1}^{L} \mathbf{C}_1^{ll} \dot{\mathbf{u}}(t)^l \tag{38}$$

Therefore, the global equilibrium equation under lth terms of Fourier series can be obtained:

$$\mathbf{K}_0^{ll}\mathbf{u}_{n+1}^l + \mathbf{K}_1^{ll}\mathbf{u}_{n+1}^l + \mathbf{K}_2^{ll}\mathbf{u}_{1\sim n}^l + \mathbf{C}^{ll}\dot{\mathbf{u}}_{n+1}^l + \mathbf{M}^{ll}\ddot{\mathbf{u}}_{n+1}^l$$
$$= \mathbf{F}_b^l + \mathbf{F}_{Ln+1}^l + \mathbf{K}_3^{ll}\mathbf{u}_{n+1}^l + \mathbf{C}_1^{ll}\dot{\mathbf{u}}_{n+1}^l \tag{39}$$

It can be found that only $\mathbf{u}_{n+1}^l$, $\dot{\mathbf{u}}_{n+1}^l$ and $\ddot{\mathbf{u}}_{n+1}^l$ are unknown variables in this equation.

Dividing time t into n equal parts, let the subscripts of variables at each time be $1 \sim n+1$. For the initial moment, assuming $\dot{\mathbf{u}}_1^l = 0$ and $\ddot{\mathbf{u}}_1^l = 0$, the $\mathbf{u}_1^l$ can be solved. Then, using Newmark-beta method (Deü et al. 2008) as follows:

$$\dot{\mathbf{u}}_{n+1}^l = \dot{\mathbf{u}}_n^l + [(1-\alpha)\ddot{\mathbf{u}}_n^l + \alpha\ddot{\mathbf{u}}_{n+1}^l]\Delta t$$
$$\mathbf{u}_{n+1}^l = \mathbf{u}_n^l + \dot{\mathbf{u}}_n^l \Delta t + [(0.5-\beta)\ddot{\mathbf{u}}_n^l + \beta\ddot{\mathbf{u}}_{n+1}^l]\Delta t^2 \tag{40}$$

Because the time increment Δt usually is tiny, the acceleration in each step can be assumed as constant, which means $\alpha = 0.5$ and $\beta = 0.25$. Therefore, the velocity and acceleration at time t can be obtained as:

$$\ddot{\mathbf{u}}_{n+1}^l = \frac{4}{\Delta t^2}(\mathbf{u}_{n+1}^l - \mathbf{u}_n^l) - \frac{4}{\Delta t}\dot{\mathbf{u}}_n^l - \ddot{\mathbf{u}}_n^l$$
$$\dot{\mathbf{u}}_{n+1}^l = \frac{2}{\Delta t}(\mathbf{u}_{n+1}^l - \mathbf{u}_n^l) - \dot{\mathbf{u}}_n^l \tag{41}$$

Substituting Equation (41) into Equation (39), the only unknown variable $\mathbf{u}_{n+1}^l$ could be calculated. Further, repeat the above iterations to solve the entire dynamic process.

3.6. Developing the calculation program

Based on the proposed method, a program named SAPAVE was developed in MATLAB. Considering that computation
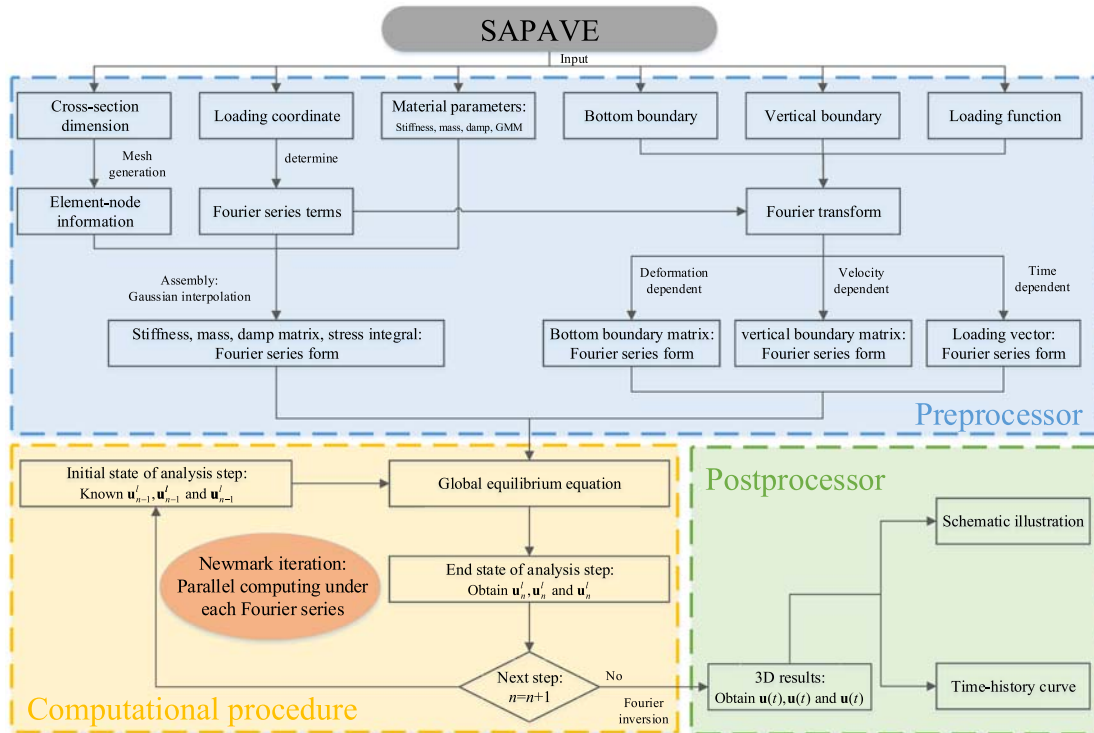

Figure 5. The flow diagram of the SAPAVE program.

Table 1. Pavement structural and material properties in case analysis.

Layer	Thickness (cm)	E (MPa)	v	ρ (kg/m³)	Rayleigh coefficients α	Rayleigh coefficients β
Surface	20	Table 2	0.3	2400	/	/
Base	20	1500	0.35	2300	1.04	5.59e-3
Subbase	40	500	0.35	2200	1.04	5.59e-3
Soil	200	100	0.45	2100	1.04	5.59e-3

Table 2. The Prony series for asphalt layer (at 30℃).

T_i (s)	∞	1	0.1	0.01	10^{-3}	10^{-4}	10^{-5}	10^{-6}
E_i (MPa)	128	536.6	945.1	2565	4221	4731	3942	2739

time is mainly derived from the matrix calculation in the equilibrium equations, MATLAB is selected for programming in this study for its excellent ability of matrix computing. This program consists of three sections: a preprocessor, a computational procedure, and a postprocessor. The flow diagram is illustrated in Figure 5.

The preprocessor generates corresponding matrixes and vectors according to the inputting parameters. Matrix integrals of each element are calculated by four-node Gaussian interpolation. Then assemble them into global matrixes based on the element number. The loading integral is assembled to the corresponding node in the vector according to the acting position.

The computational procedure can use parallel computation (Luszczek 2009) under each Fourier series term, because of which iteration computation is independent. This technology can further enhance the calculation efficiency by making full use of CPU threads, but only Intel CPU supports this function currently.

The postprocessor utilises the Fourier inversion transform to get the displacement in 3D space. Then use the displacement-strain–stress relationship to obtain all pavement responses. The response nephogram or time-history curve can be obtained by specifying the coordinate.

4. Program validation

A typical asphalt pavement was modeled using SAFEM to verify its accuracy and efficiency. Further, the results and computing cost were compared with the ones from 3D FEM in ABAQUS.

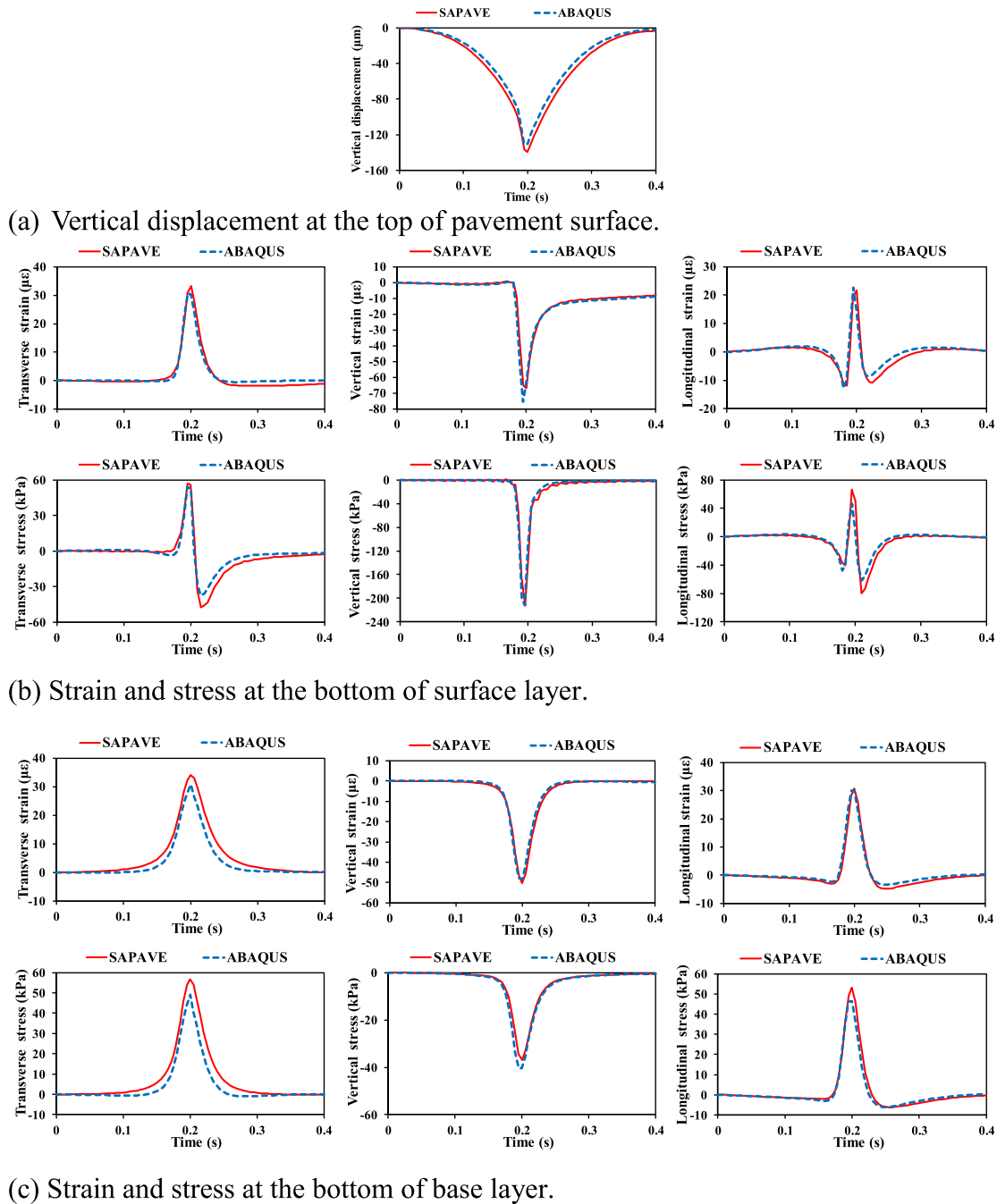## 4.1. Pavement structure and material properties

A pavement model with four structural layers was developed with the pavement structure and material properties listed in Table 1. This model has 10-m depth along the z coordinate and 2-m width along the x coordinate. The Prony series of the GMM for asphalt layer is defined as Table 2, which was obtained from the master curve of dynamic modulus measured for the asphalt mixture with PG 64-16.

The 3D model meshed in ABAQUS is illustrated in Figure 6. The load in SAPAVE and ABAQUS is assumed as square-shape loading with side length of 20 cm, and the uniformly distributed contact pressure is 0.7 MPa. The load moves along the center of pavement surface with a speed of 20 m/s, and its initial z coordinate is 1.0 m. The 2D meshing in SAPAVE adopts the same as the ABAQUS, while the driving direction adopts the Fourier series to interpolate. As illustrated in Figure 7, with the increase of Fourier series terms, the fitting is closer to the load function, but the computation time increases proportionally. Therefore, to balance computation efficiency and accuracy, 66 terms were appropriate by step-by-step verification.

4.2. Initial state setting

Setting appropriate initial state is vital for dynamic analysis, while incorrect initial state would cause unreal vibrations in the systems, leading to the iterative divergence. For SAPAVE, the static response generated by the load at the initial position
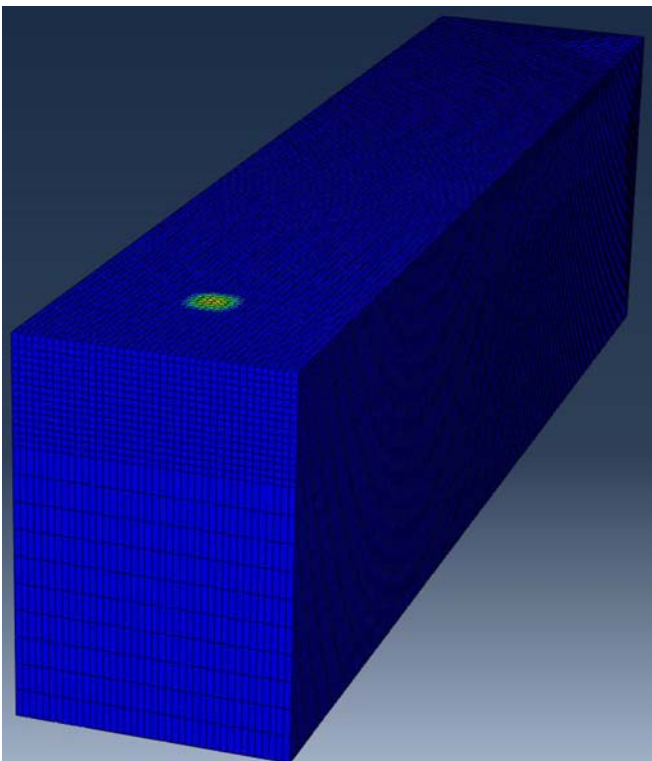
Figure 6. The 3D FE model of the pavement generated in ABAQUS.
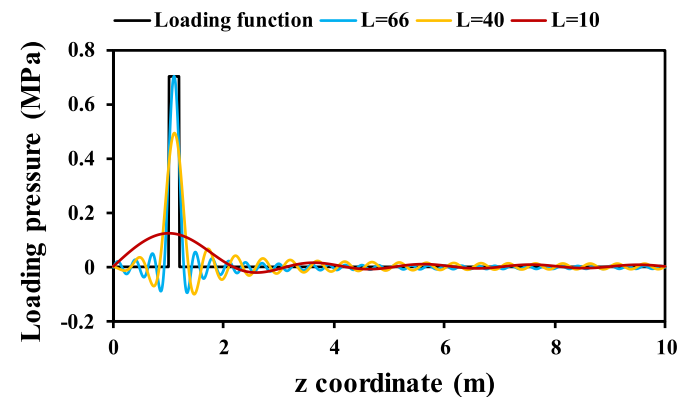
Figure 7. The Fourier series expansion results of different terms.

(a) Vertical displacement at the top of pavement surface.

(b) Strain and stress at the bottom of surface layer.

(c) Strain and stress at the bottom of base layer.

Figure 8. Comparison of the results between SAPAVE and ABAQUS. (a) Vertical displacement at the top of pavement surface. (b) Strain and stress at the bottom of surface layer. (c) Strain and stress at the bottom of base layer.

is set as the initial state. Therefore, $\mathbf{u}(0)$ can be obtained and $\dot{\mathbf{u}}(0)$ and $\ddot{\mathbf{u}}(0)$ are set as zero. Moreover, the similar initial state was established in ABAQUS by setting a preliminary analysis step, which maintains the load at the initial position for one second. Setting this step is because the suddenly applied load can cause vibrations; while keeping the load for one second can stabilise the structure.

4.3. Analytical results

The dynamic analysis lasts for 0.4s with time increment of 0.005s. Select the model center as the analytical object. The time-history curves of representative responses of the model

midpoint are shown in Figure 8, including vertical displacement at the top of pavement surface, strains and stresses at the bottom of surface and base layers. The results shows that the responses obtained from SAPAVE have good agreements with those of ABAQUS.

Moreover, the cross-section distributions of stress and strain at 0.2 s generated in SAPAVE are illustrated in Figure 9. As expected, the tension state was found concentrated on the bottom of the surface and base while compression on the pavement surface. The vertical strain and stress decayed with the depth in the surface and base layer. These results are generally consistent with other researches (Li et al. 2016, Xiang and Wang 2018).
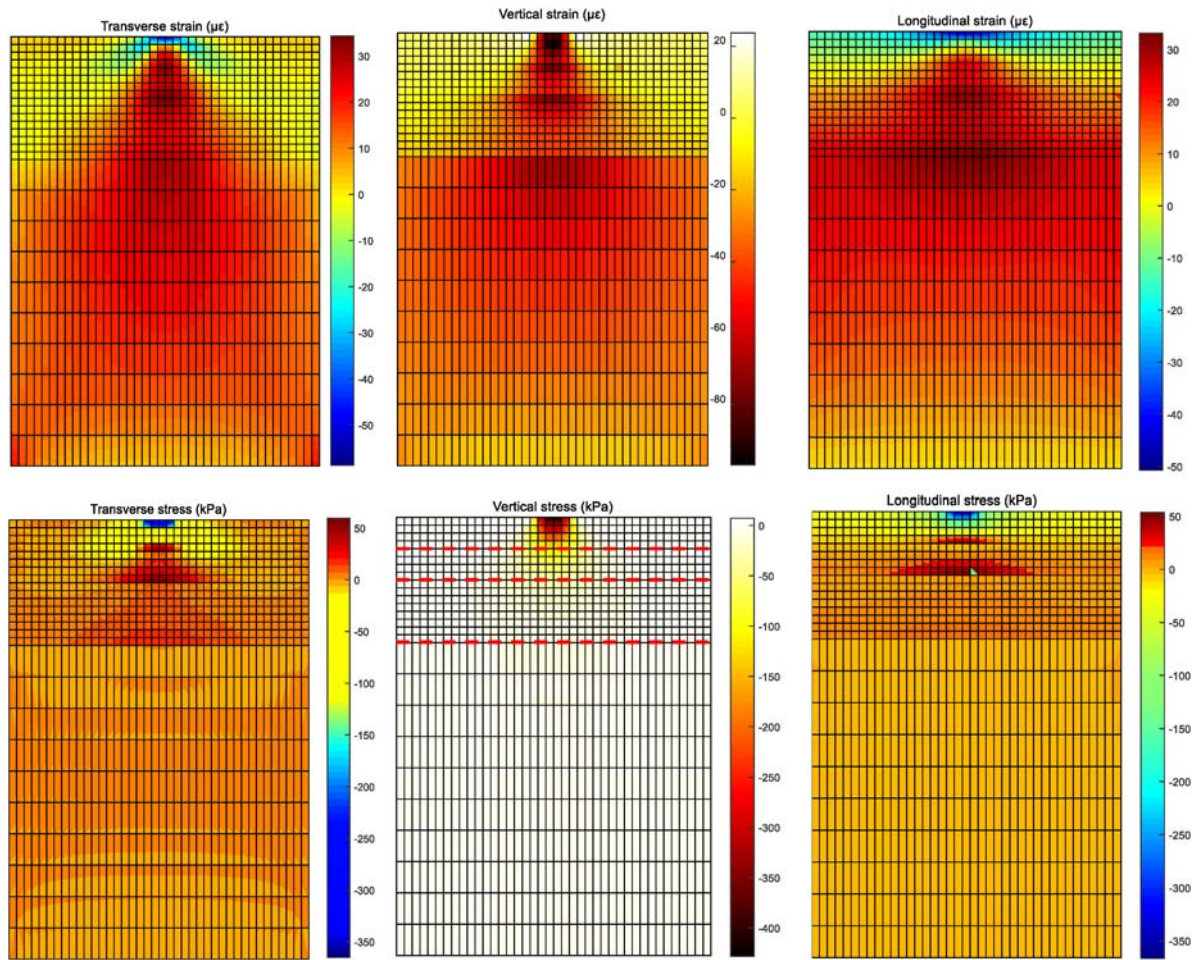
Figure 9. The cross-section ($z = 5.0$ m) distributions of stresses and strains at 0.2 s.
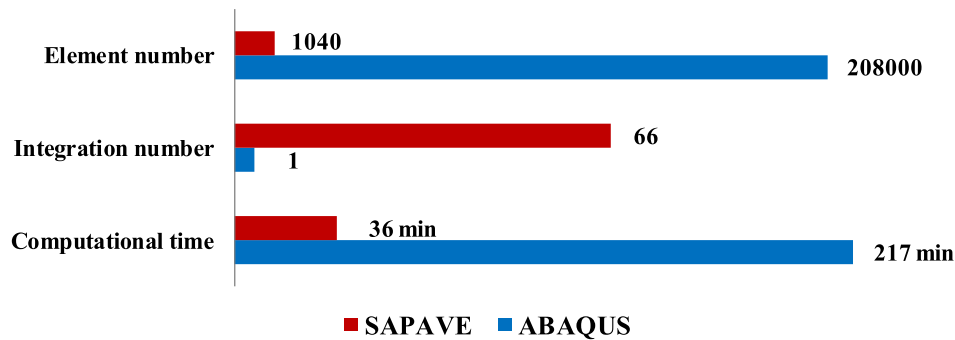

Figure 10. Comparison of computational requirements between SAPAVE and ABAQUS.

Two models were operated on a computer with one Intel Xeon E5-2630 CPU and 128G ROM, and the multicore computing used all 12 cores of the CPU. The computational requirements are illustrated in Figure 10. The computational time cost by SAPAVE is 36 min, which is only 16% of the time using ABAQUS.

5. Program application

The impact of vehicle speed on dynamic pavement responses is analyzed to verify the applicability of SAPAVE. The vehicle speeds were set as 10, 20, and 40 m/s, and the material parameters were the same as the previous section. Besides, the time increment was set as 0.01, 0.005, and 0.0025s, respectively. This setting had two benefits. First, it can ensured the loading positions of three situations were the same in each analytical step and contained the position corresponding to maximum responses ($z = 5$ m). Second, the number of analytical steps was the same in the three processes, which controlled the error differences generated by the number of iteration. Moreover, to explore the effect of viscoelasticity of asphalt mixture on dynamic response, the surface was set as an elastic

layer with elastic modulus of 3500 MPa to conduct comparative analysis. The time-history curves of several representative responses are illustrated in Figure 11.

The vertical displacement and strain of viscoelastic analysis decrease with increasing speed, and there is a process of creep recovery when the load leaves. However, these elastic analysis responses barely change with speed and return to the original state quickly when the load goes. This phenomenon is because the viscoelastic response relates to the loading time (Sun et al. 2018), and slower speed means longer loading time, increasing the creep deformation. However, elastic materials do not have this behavior.

There is tension and compression transformation of transverse stress in viscoelastic analysis while not in dynamic analysis. This transformation is because the load function first causes tension stress, and the viscoelasticity would cause compression stress by creep recovery after the load leaves (Wang et al. 2020). However, elastic material will directly return to the original state after unloading. It can also explain why the longitudinal stress in viscoelastic analysis has bigger tension and compression transformation than the one in elastic analysis.

Compared with the results monitored in field asphalt pavement (Chatti et al. 1996, Ai et al. 2017), viscoelastic analysis results are closer to the practical situation. Moreover, the relationship between dynamic response and vehicle speed obtained by SAPAVE is similar to the field measurement results.

Figure 11. Comparison of the results between viscoelastic and elastic analyses.

6. Conclusions

This study proposed improved model formulation for SAFEM with modified artificial boundaries for dynamic viscoelastic analysis of flexible pavement. A program named SAPAVE was developed in MATLAB to achieve this simulation. For typical pavement structure, the analysis results were found in good agreements with those from 3D model in ABAQUS. The SAPAVE has significant advantage in computation time. The calculated pavement responses from viscoelastic analysis were found closer to field measurements. The elastic analysis cannot represent creep recovery and time-dependent behavior of asphalt layer responses. It was also found that viscoelastic pavement responses decreased with speed, while elastic responses hardly changed.

Further studies can be conducted to enhance computation efficiency and accuracy of SAPAVE. For example, the integer-order constitutive model can be replaced by the fractional-order ones with less viscoelastic parameters. This modification will enhance efficiency by reducing the number of iteration modules. Besides, the temperature and moisture gradient of pavement structure can be considered in the model. The ultimate goal is to develop an efficient program for flexible pavement design and evaluation in simple engineering applications.

Declaration of interest statement

We declare that we do not have any commercial or associative interest that represents a conflict of interest in connection with the work submitted.

Disclosure statement

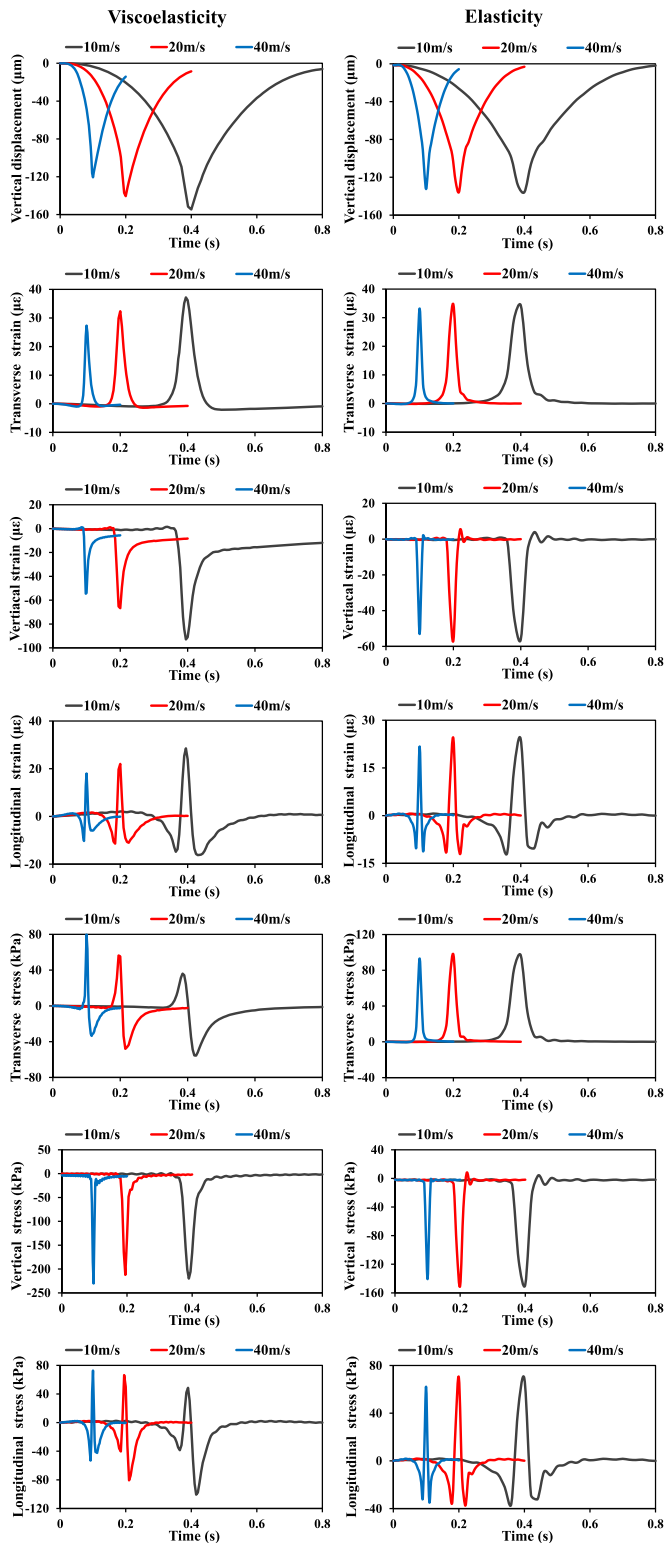No potential conflict of interest was reported by the authors.

Funding

ORCID

Kairen Shen http://orcid.org/0000-0002-9833-9955
Hao Wang http://orcid.org/0000-0001-8666-6900
Hanyu Zhang http://orcid.org/0000-0001-5181-4619
Xianhua Chen http://orcid.org/0000-0001-8395-5002

References

Ai, C., et al., 2017. Analysis of measured strain response of asphalt pavements and relevant prediction models. *International Journal of Pavement Engineering*, 18 (12), 1089–1097.

Beskou, N.D., Hatzigeorgiou, G.D., and Theodorakopoulos, D.D, 2016a. Dynamic inelastic analysis of 3-D flexible pavements under moving vehicles: A unified FEM treatment. *Soil Dynamics and Earthquake Engineering*, 90, 420–431.

Beskou, N.D., Hatzigeorgiou, G.D., and Theodorakopoulos, D.D, 2016b. Dynamic elastic analysis of 3-D flexible pavements under moving vehicles: A unified FEM treatment. *Soil Dynamics and Earthquake Engineering*, 82, 63–72.

Chatti, K., et al., 1996. Field investigation into effects of vehicle speed and tire pressure on asphalt concrete pavement strains. *Transportation Research Record*, 1539, 66–71.

Chen, G., and Russell, D.L, 1982. A mathematical model for linear elastic systems with structural damping. *Quarterly of Applied Mathematics*, 39 (4), 433–454.

de Araújo, P.C., et al., 2010. Dynamic viscoelastic analysis of asphalt pavements using a finite element formulation. *Road Materials and Pavement Design*, 11 (2), 409–433.

Deü, J.F., Galucio, A.C., and Ohayon, R, 2008. Dynamic responses of flexible-link mechanisms with passive/active damping treatment. *Computers and Structures*, 86 (3–5), 258–265.

Hatzigeorgiou, G.D., and Beskos, D.E, 2010. Soil-structure interaction effects on seismic inelastic analysis of 3-D tunnels. *Soil Dynamics and Earthquake Engineering*, 30 (9), 851–861.

Helwany, S., Dyer, J., and Leidy, J, 1998. Finite-element analyses of flexible pavements. *Journal of Transportation Engineering-ASCE*, 124 (5), 491–499.

Hu, S., et al., 2008. SA_crackrro: New finite element analysis tool for pavement crack propagation. *Transportation Research Record: Journal of the Transportation Research Board*, 2068 (1), 10–19.

Huang, Y.H., 2004. Pavement Analysis and Design, Prentice Hall: Kentucky.

Jooste, F.J, 2002. Flexible pavement response evaluation using the semi-analytical finite element method. *Road Materials and Pavement Design*, 3 (2), 211–225.

Kaliske, M., and Rothert, H, 1997. Formulation and implementation of three-dimensional viscoelasticity at small and finite strains. *Computational Mechanics*, 19 (3), 228–239.

Kalogiratou, Z., and Simos, T.E, 2003. Newton-Cotes formulae for long-time integration. *Journal of Computational and Applied Mathematics*, 158 (1), 75–82.

Kim, J, 2011. General viscoelastic solutions for multilayered systems subjected to static and moving loads. *Journal of Materials in Civil Engineering*, 23 (7), 1007–1016.

Li, S., Guo, Z., and Yang, Y, 2016. Dynamic viscoelastic response of an instrumented asphalt pavement under various axles with non-uniform stress distribution. *Road Materials and Pavement Design*, 17 (2), 446–465.

Liu, P., et al., 2017. Application of dynamic analysis in semi-analytical finite element method. *Materials*, 10 (9), 1010–1022.

Liu, P., et al., 2018a. Application of semi-analytical finite element method to evaluate asphalt pavement bearing capacity. *International Journal of Pavement Engineering*, 19 (6), 479–488.

Liu, P., et al., 2018b. Application of linear viscoelastic properties in Semianalytical finite element method with Recursive time Integration to Analyze asphalt pavement structure. *Advances in Civil Engineering*, 2018, Article ID 9045820, 15 pages.

Liu, P., Wang, D., and Oeser, M, 2015. Application of semi-analytical finite element method coupled with infinite element for analysis of asphalt pavement structural response. *Journal of Traffic and Transportation Engineering (English Edition)*, 2 (1), 48–58.

Luszczek, P, 2009. Parallel programming in MATLAB. *International Journal of High Performance Computing Applications*, 23 (3), 277–283.

Markovitz, H, 1977. Boltzmann and the beginnings of linear viscoelasticity. *Transactions of the Society of Rheology*, 21 (3), 381–398.

Moita, J.S., et al., 2011. A finite element model for the analysis of viscoelastic sandwich structures. *Computers and Structures*, 89 (21–22), 1874–1881.

Mulliken, J.S., and Karabalis, D.L, 1998. Discrete model for dynamic through-the-soil coupling of 3-D foundations and structures. *Earthquake Engineering and Structural Dynamics*, 27 (7), 687–710.

Myers, L.A., Roque, R., and Birgisson, B, 2001. Use of Two-dimensional finite element analysis to represent Bending response of asphalt pavement structures. *International Journal of Pavement Engineering*, 2 (3), 201–214.

Saad, B., Mitri, H., and Poorooshasb, H, 2005. Three-dimensional dynamic analysis of flexible conventional pavement foundation. *Journal of Transportation Engineering*, 131 (6), 460–469.

Sun, Y., et al., 2018. Viscoelastic mechanical responses of HMAP under moving load. *Materials*, 11 (12), 1–19.

Tolstov, G.P., 2012. *Fourier series*. Martino Fine Books: Eastford.

Wang, H., et al., 2020. Flexible pavement response analysis under dynamic loading at different vehicle speeds and pavement surface Roughness conditions. *Journal of Transportation Engineering Part B: Pavements*, 146 (3), 1–10.

Wu, Z., Hu, S., and Zhou, F, 2014. Prediction of stress intensity factors in pavement cracking with neural networks based on semi-analytical FEA. *Expert Systems with Applications*, 41 (4), 1021–1030.

Xiang, P., and Wang, H, 2018. Optical fibre-based sensors for distributed strain monitoring of asphalt pavements. *International Journal of Pavement Engineering*, 19 (9), 842–850.

Zienkiewicz, O.C. and Taylor, R.L., 2005. *The finite element method for solid and structural mechanics*. Elsevier Butterworth-Heinemann: Oxford.

Zienkiewicz, O.C., and Too, J.J.M, 1972. Finite prism in analysis of thick simply supported bridge boxes. *Proceedings of the Institution of Civil Engineers, Part 2: Research and Theory*, 53 (Sep), 147–172.